Best Available Copy

NAVAL POSTGRADUATE SCHOOL
Monterey, California

DTIC
SELECTE
JAN 3 1 1994
S B D

THESIS

FAR ULTRAVIOLET IMAGES OF THE NIGHTTIME
IONOSPHERE

by

Thomas P. Hekman

September 1993

Thesis Advisor: David D. Cleary
Second Reader: Suntharalingam Gnanalingam

REPORT DOCUMENTATION PAGE	Form Approved OMB No. 0704

Public reporting burden for this collection of information is estimated to average 1 hour per response, including the time for reviewing instruction, searching existing data sources, gathering and maintaining the data needed, and completing and reviewing the collection of information. Send comments regarding this burden estimate or any other aspect of this collection of information, including suggestions for reducing this burden, to Washingon headquarters Services, Directorate for Information Operations and Reports, 1215 Jefferson Davis Highway, Suite 1204, Arlington, VA 22202-4302, and to the Office of Management and Budget, Paperwork Reduction Project (0704-0188) Washington DC 20503.

AGENCY USE ONLY (Leave blank)	2. REPORT DATE 23 September 1993.	REPORT TYPE AND DATES COVERED Master's Thesis

TITLE AND SUBTITLE FAR ULTRAVIOLET IMAGES OF THE NIGHTIME IONOSPHERE	FUNDING NUMBERS
AUTHOR(S) Thomas P. Hekman, LT USN	
PERFORMING ORGANIZATION NAME(S) AND ADDRESS(ES) Naval Postgraduate School Monterey CA 93943-5000	PERFORMING ORGANIZATION REPORT NUMBER
SPONSORING/MONITORING AGENCY NAME(S) AND ADDRESS(ES)	SPONSORING/MONITORING AGENCY REPORT NUMBER

11. SUPPLEMENTARY NOTES The views expressed in this thesis are those of the author and do not reflect the official policy or position of the Department of Defense or the U.S. Government.

12a. DISTRIBUTION/AVAILABILITY STATEMENT Approved for public release; distribution is unlimited.	12b. DISTRIBUTION CODE *A

ABSTRACT (maximum 200 words)

The Naval Research Laboratory's Far Ultraviolet Cameras Experiment is part of an ongoing project to develop a means for real time space based monitoring of the upper atmosphere. The purpose of this paper is to develop a method by which useable data can be extracted from the images obtained from the cameras. The required output is an intensity profile of the light in the band of the camera as a function of observation zenith angle. From this data future analysis can be done to determine the spatial distribution and density of the upper atmosphere. The long term application of this project is to develop a method for using space based imaging of the ionosphere to provide real time radio frequency propagation analysis.

14. SUBJECT TERMS Far Ultraviolet, Ultraviolet, Ionosphere, Atmosphere, Space Based Imaging.	NUMBER OF PAGES 66
	PRICE CODE

SECURITY CLASSIFICATION OF REPORT Unclassified	SECURITY CLASSIFICATION OF THIS PAGE Unclassified	SECURITY CLASSIFICATION OF ABSTRACT Unclassified	LIMITATION OF ABSTRACT UL

NSN 7540-01-280-5500

Standard Form 298 (Rev. 2-89)
Prescribed by ANSI Std. 239-18

FAR ULTRAVIOLET IMAGES OF THE NIGHTIME
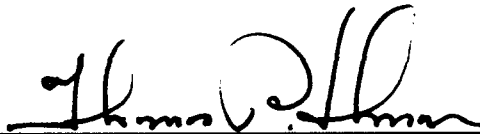IONOSPHERE

by

Thomas P. Hekman
Lieutenant, United States Navy
B.A., Virginia Polytechnic Institute, 1986

Submitted in partial fulfillment
of the requirements for the degree of

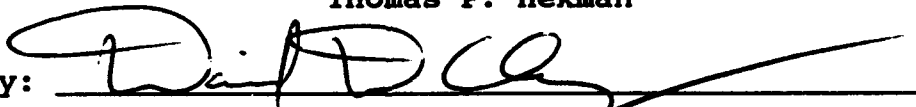MASTER OF SCIENCE IN SYSTEMS ENGINEERING
(ELECTRONIC WARFARE)
from the

NAVAL POSTGRADUATE SCHOOL
September 1993

Author: _____
Thomas P. Hekman

Approved by: _____
David D. Cleary, Thesis Advisor

_____
Suntharalingam Ghanalingam, Second Reader

_____
Jeffrey B. Knorr, Chairman
Electronic Warfare Academic Group

ii

ABSTRACT

The Naval Research Laboratory's Far Ultraviolet Cameras Experiment is part of an ongoing project to develop a means for real time space based monitoring of the upper atmosphere. The purpose of this paper is to develop a method by which useable data can be extracted from the images obtained by the cameras. The required output is an intensity profile of the light in the band of the camera as a function of the observer zenith angle. From this data future analysis can be done to determine the spatial distribution and density of the constituent species of the upper atmosphere. The long term application of this project is to develop a method for using space based imaging of the ionosphere to provide real time radio frequency propagation analysis.

iii

TABLE OF CONTENTS

I. INTRODUCTION

A. BACKGROUND

The purpose of this thesis is to develop a means for analyzing images obtained by two far ultraviolet cameras developed by the Naval Research Laboratory. The Far Ultraviolet Cameras Experiment was part of the Air Force Program 675 (AFP-675) payload flown aboard space shuttle mission STS-39 between 28 April and 6 May 1991. AFP-675 consisted of the following instruments:

1) CIRRIS - Cryogenic Infrared Radiance Instrumentation for Shuttle. This instrument measured spatial, spectral, and temporal variations in the Earth's limb and aurora between 2.5 and 25μm.

2) FAR UV - Far Ultraviolet Cameras. Designed to image near Earth and celestial ultraviolet sources, including airglow, aurora, stars, nebulae, shuttle glow, shuttle thruster firings, and shuttle H_2O discharges. This paper will address the airglow portion of this experiment.

1

3) URA - Uniformly Redundant Array. Demonstrated coded aperture imaging of x-ray emissions from celestial targets.

4) HUP - Horizon Ultraviolet Program. Measures spatial and spectral ultraviolet characterisitics of the Earth's horizon.

5) QINMS - Quadrupole Ion and Neutral Mass Spectrometer. Monitors contamination in the shuttle environment and provides input to CIRRIS. (STS-39 PID)

B. FAR ULTRAVIOLET CAMERAS EXPERIMENT

The objectives of the Far Ultraviolet Cameras Experiment included; far ultraviolet (1050-2000Å) measurements of the Earth's upper atmosphere, celestial bodies including diffuse background sources, and the shuttle environment. The shuttle enviroment study included shuttle glow, and thruster firings. Upper atmosphere observations include night horizon airglow and the auroras. The purpose of these observations was to demonstrate a means for remote sensing of atomic oxygen and NO density versus altitude in the upper atmosphere. The night airglow observations were specificaly designed to demonstrate the ability to conduct remote sensing of the night ionosphere. The results of this experiment will be used to support future

space based real time remote sensing of the night ionosphere. This will be attempted by the Global Imaging Monitor of the Ionosphere (GIMI) project scheduled to be deployed aboard the ARGOS P-91 satellite. GIMI will use similar cameras but will utilize CCD detectors instead of electrographic film to provide a real time digitized RF output. This output will be processed at a ground station to determine an altitude profile of the atmosphere. The work done in this thesis will provide the basis for deriving altitude and intensity from the photographs and will provide the background material necessary for further research on this project. The methods used to analyze the images from the AFP-675 project should be similar to the methods required to analyze the GIMI output; therefore, the methods covered herein should support GIMI as well as AFP-675. (Carruthers, 1992)

C. THESIS OUTLINE AND OBJECTIVES

In addition to the purpose stated above, this paper is intended to provide necessary background information for follow on work. The paper is organized as follows.

Chapter I: This chapter provides general background information on the Far Ultraviolet Cameras Experiment and future applications of work associated with the project.

Chapter II: This chapter provides background information on the structure of the ionosphere, chemical and dynamical

3

processes in the ionosphere, and a brief introduction to the night airglow phonemena. Topics covered include diffusion mechanism, density scale height, ionization rates, and photochemical equilibrium.

Chapter III: Provides a detailed description of the Far UV Cameras and the methods used to reduce the image data into data files.

Chapter IV: Covers data analysis performed as part of this thesis. Includes a description of the means by which shuttle position and attitude were determined and details the programs used to interpret the image data files. This section includes graphs of intensity versus observation zenith angle obtained from the images.

Chapter V: Contains a summary of findings and topics for future NPS students to research.

II.   BACKGROUND

A.   THE UPPER ATMOSPHERE

1.   General Description

a.   Temperature Structure

The upper atmosphere can be described in many ways. The most common means of describing the layers of the atmosphere is by the temperature profile. Figure (1) shows a theoretical plot of temperature versus altitude and identifies the various layers.
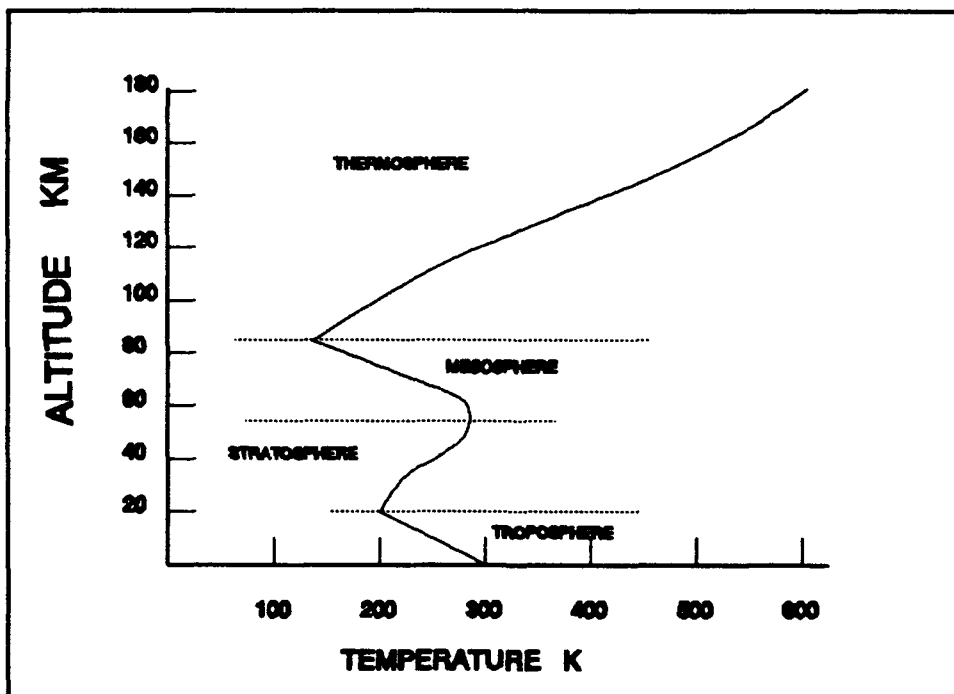
Figure 1: Temperature Profile of atmospheric layers.

In the thermosphere the sun's radiation in the vacuum ultraviolet region is absorbed by atomic and molecular nitrogen and oxygen. This absorption generates heat, as altitude decreases less vacuum ultraviolet radiation reaches the atmosphere resulting in lower temperatures. This explains the positive temperature gradient in the thermosphere. The temperature in the thermosphere reaches a minimum at about 85 km (The mesopause). Below this point ozone becomes an important constituent and it absorbs longer solar radiation wavelengths (2000 -3000Å). From 85 km to about 50 km the increasing density of ozone causes a temperature increase with decreasing altitude. Also absorbed by ozone is the Lyman-α radiation at 1216Å which passes through the nitrogen and atomic oxygen to an altitude of about 65 km. At 50 km enough of the 2000 - 3000Å and Lyman-α radiation has been removed to allow a positive temperature gradient to form again even though the density of ozone continues to increase.

This thesis will deal primarily with the atmosphere above 100 km. Therefore our discussions will be limited to the thermosphere. A profile of thermospheric temperature is shown in Figure (2). This profile was calculated using the equation:

$$T = T_\infty - (T_\infty - T_{120}) e^{-s(Z-120)} \qquad (1)$$

6

where T_∞ is the temperature at the outer edge of the atmosphere and T_{120} is the temperature at altitude 120 km, z is altitude, and s is .0255 km^{-1}. The figure shows temperature calculated in 2km increments from 120 to 300 km. T_∞ can vary from 1000K and 1800K depending on the solar cycle. 1500K is used in this calculation. A value of 200K is used for T_{120}.

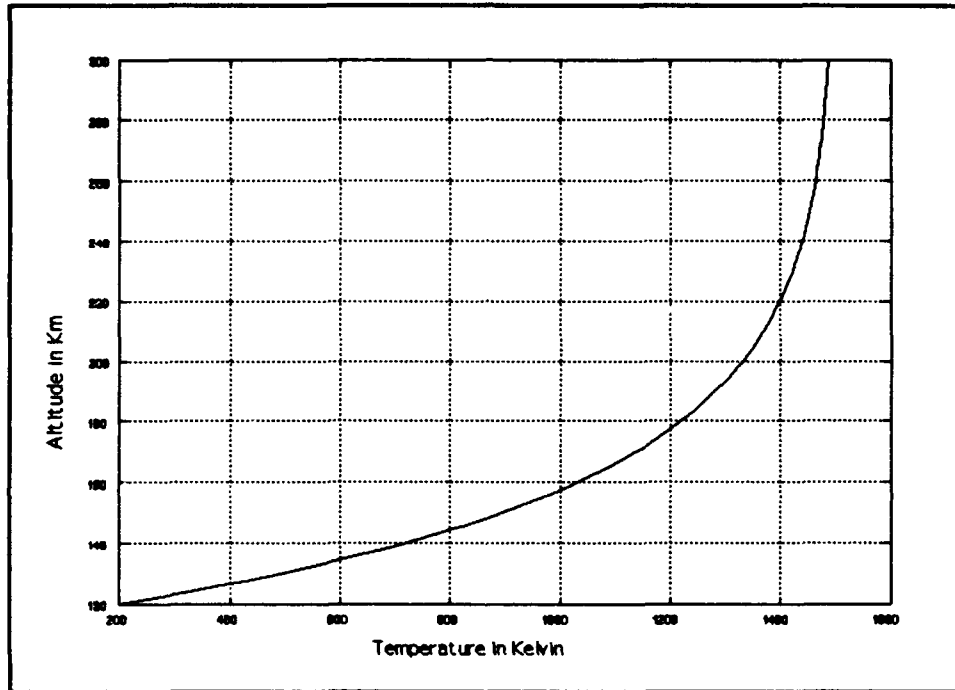**Figure 2:** Temperature vs Altitude from 120-300 km. T_∞ = 1500 K, T_{120} = 200 K

b. Diffusion Structure

Another means of describing the atmosphere is by the mechanism of diffusion which dominates at a given altitude. Their are two basic mechanisms of diffusion for the neutral atmosphere, molecular diffusion, and eddy diffusion. Eddy diffusion is the turbulent mixing of parcels of air in a

given region. This is the dominant method in the troposphere, stratosphere, and mesosphere where the atmosphere is more dense and acts like a fluid. In the troposphere and mesosphere strong negative temperature gradients allow the easy rise of warm air and sinking of cooler air. Alternatively, the dominant diffusion method in the thermosphere is molecular diffusion. In this region the strong positive temperature gradient inhibits the vertical mixing of the atmosphere. The one exception to this is the region between 85 km and 120 km where atmospheric tides create strong vertical wind shears in the prevailing horizontal winds. The stratosphere has a temperature gradient similar to that of the thermosphere; here the molecular diffusion rate approaches the eddy diffusion rate but eddy diffusion still dominates.

As a result, the atmosphere can be divided into two diffusion regions; the homosphere and the heterosphere. The homosphere is the region below 90 km and has a nearly constant mean molecular mass. The region above 115 km is called the heterosphere and is characterized by the mean molecular mass decreasing with altitude due to varying scale heights. (Scale height will be covered in Chapter III.) Figure (3) gives a general indication of diffusion types and rates versus altitude, and illustrates the two regions. The figure illustrates the crossover point at 115 km and shows the variable nature of the eddy diffusion term. Between 90 and
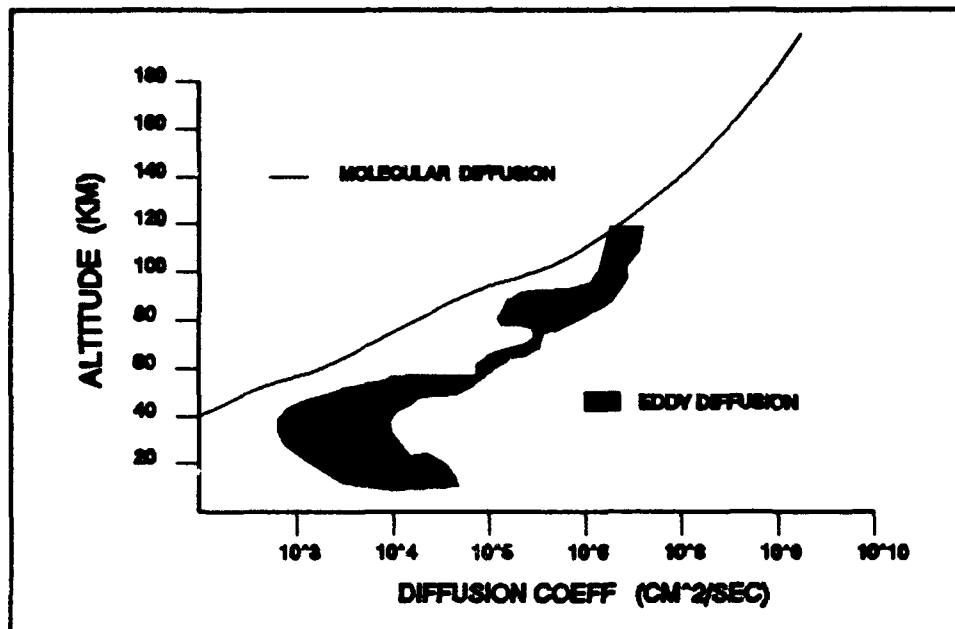
Figure 3: Eddy vs Molecular Diffusion for N2. (Heicklen, pg 4)

115 km molecular diffusion and eddy diffusion are comparable as illustrated in Figure (3).

c. The Ionosphere

The ionosphere is so named because of the ionization of its constituent elements by solar radiation. The ionosphere is described by regions of varying electron density. The ionoshere is divided into four distinct regions; the D region which is lowest in altitude, the E region, the F_1 region, and the F_2 region which is the highest. The D region extends from about 50 km to 90 km blending in with the lower region of the E region with no sharp boundary. The D region experiences total solar control. It builds rapidly in the

morning, maximizes near local noon, and rapidly diminishes at sunset. The E region extends from the top of the D region to the bottom of the F region, approximately 90 - 130 km. The electron density of the E region peaks at about 110 km. The E region is very predictable reaching a maximum slightly later in the day than the D region. The E region does not disappear at night but does reach a minimum density. The F region is the highest ionospheric region. The F region extends upward from about 130 km and has no clearly defined upper limit. During daylight the F region splits into two distinct layers, F_1 and F_2. The F_1 layer is the lower and less dense layer. It is controlled directly by solar activity and disappears at night blending into a single F layer. The F_2 region is the highest and most dense layer with a daytime peak altitude of approximately 300 km. The F_2 region is the most variable of all the ionospheric regions. The F region reaches maximum density a few hours later than the D or E regions and does not disappear at night. This is due to the substantially lower loss rate of the constituent ions in the F region compared to those in the D and E regions. A graph of electron densities is given in Figure (4).

10
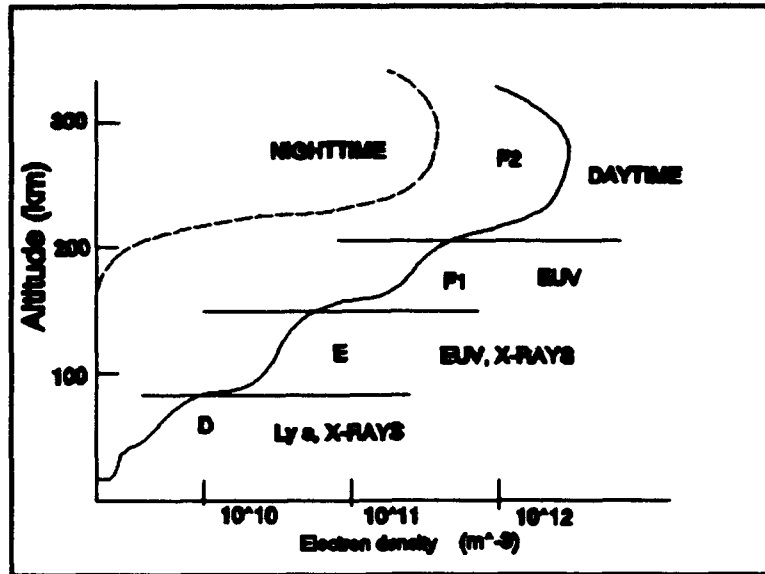
Figure 4: Day and Night Electron Densities.

2. The Mass Continuity Equation

There are several mechanisms for the production and loss of the constituent species of the ionosphere; diffusion, chemical reactions, and photoionization are the major mechanisms. The mass continuity equation describes production and loss involving these mechanisms. The one-dimensional approximation to the mass continuity equation is:

$$\frac{dn}{dt} = P - nL - \frac{\partial \Psi}{\partial z} \qquad (2)$$

11

where dn/dt is the rate of change in number density, P is the chemical production rate, L is the chemical loss rate, and n is the density of the specific species, and $\partial \Psi/dz$ represents loss due to diffusion. Each term will be discussed in detail beginning with diffusion.

a. Diffusive Equilibrium

The major neutral species (O, O_2, N_2) are primarily affected by diffusion. Chemical production and loss also occurs with these species; however, their rates are so small in comparison to the rate of diffusion that they can be ignored ($P-nL \ll \partial \Psi/dz$). A state of diffusive equilibrium exists when diffusion dominates and dn/dt = 0. This results in equation (2) reducing to:

$$0 = -\frac{\partial \Psi}{\partial z} \qquad (3)$$

From this equation it can be shown:

$$n(z) = n_o \exp^{-\frac{(Z-Z_o)}{H^*}} \qquad (4)$$

where n(z) is the number density of the species and has units of cm^{-3}. Z is the altitude at which the density is calculated and Z_o is the lower altitude limit (120 km for this paper). H^* is the density scale height and is given by:

$$H^{\circ} = \cfrac{1}{\dfrac{mg}{kT} + \left(\dfrac{1}{T}\right)\left(\dfrac{dT}{dz}\right)} \qquad (5)$$

where m is the atomic mass of the atom or molecule, g is the acceleration due to gravity, k is Boltzmann's constant, T is temperature (Kelvin), and dT/dZ is the temperature gradient. Scale height is the difference in altitude that it takes the density of a species to drop by 1/e.

b. Photochemical Equilibrium

For the major ionic (N_2^+, O_2^+, O^+, NO^+), and the minor neutral (NO, $N(^4S)$, and $N(^2D)$) species in the ionosphere, chemical reaction rates greatly exceed diffusion rates; therefore, $d\bar{Y}/dz$ <P-nL and diffusion is neglected. A state of photochemical equilibrium exists when chemistry dominates and dn/dt=0. Thus chemical production and loss rates are equal (P-nL=0) and equation (2) becomes:

$$n = \frac{P}{L} \qquad (6)$$

c. Photoionization

Photoionization by solar radiation is the primary means of ion production in the ionosphere. The highest rate of ion production results from the excitation of atoms and

molecules by solar radiation. The ionization rate (Q) of a given species is:

$$Q(z,\theta) = n(z) \sum_{\lambda} \sigma_i(\lambda) I_{\lambda}(z,\theta) \Delta\lambda \qquad (7)$$

where n(z) is the number density given above, $\sigma_i(\lambda)$ is the ionization cross section, and I_{λ} is the intensity of the solar radiation, at the wavelength λ, at the altitude z, when the solar zenith angle is θ. Each of these items is described in detail in the following paragraphs.

The intensity can be calculated using the following equation:

$$I_{\lambda}(z,\theta) = I_{\lambda}(\infty) \exp^{-\tau(z,\theta)} \qquad (8)$$

where $I_{\lambda}(\infty)$ is the intensity at the top of the atmosphere and $\tau(z,\theta)$ is the optical depth. $I_{\lambda}(\infty)$ is tabulated.

The optical depth can be calculated using the following equation:

$$\tau_{\lambda}(z,\theta) = \sum_{z} \sigma_a(\lambda) N(z,\theta) \qquad (9)$$

where $\sigma_a(\lambda)$ is the species absorption cross section at the wavelength λ and $N(z,\theta)$ is the slant column density. The optical depth is a measure of the attenuation of solar irradiance by the Earth's atmosphere. Optical depth is dependent on the specific^Xxavelength, the absorption cross section of the given species, the altitude dependent

14

concentration of the given species, and the solar zenith angle. Where optical depth reaches unity ($\tau=1$), a noticeable drop in intensity ($I_\lambda(Z)$) occurs. This drop is illustrated in Figure(5).
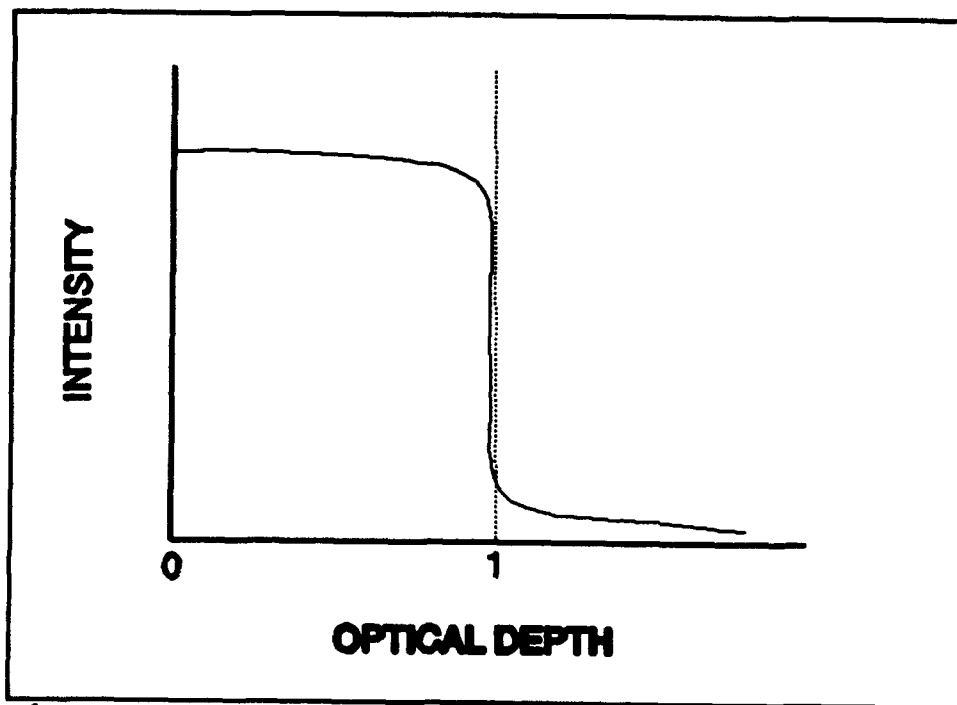
Figure 5: Optical Depth vs Intensity.

The column density, $N(z,\theta)$, of the species and can be calculated from the number density using the following equation:

$$N(z,\theta) = \int_z^\infty n(z)\,\frac{dz}{\cos\theta} \tag{10}$$

where θ is the angle between the direction of the solar radiation and the vertical axis, generally called the solar zenith angle.

3. Chemical Production and Loss in the Ionosphere

Using the ionization rate described above, the mass continuity equation, and using tabulated equations for the production and loss of ions in the ionosphere, it is possible to calculate the density of each ionic species. The constants associated with these equations for production and loss are given in Appendix A. Equations for determining the density of the major (N_2^+, O_2^+, O^+, NO^+) and the minor (NO, $N(^4S)$, and $N(^2D)$) constituents are given below. The reaction coefficients are listed in Appendix A.

The following reactions produce O^+:

$$O + h\nu \rightarrow O^+ + e \qquad\qquad (11)$$

$$N_2^+ + O \rightarrow O^+ + N_2 \qquad\qquad (12)$$
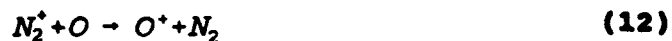
The following equations account for the loss of O^+:

$$O^+ + N_2 \rightarrow NO^+ + N(^4S) \qquad\qquad (13)$$

16

$$O^+ + O_2 \rightarrow O_2^+ + O \qquad (14)$$

Using equation (8) and reactions (11) through (14), the density of O^+ can be calculated using the following equation:

$$[O^+] = \frac{Q_{(O)} + K_{17b}[N_2^+][O]}{K_{20}[N_2] + K_{21}[O_2]} \qquad (15)$$

where Q is the ionization rate discussed above. The subscript following the reaction coefficient K is the reaction number listed in Appendix A, and [X] is the number density of species X. Similar calculations can be done for NO^+, NO, $N(^4S)$, $N(^2D)$, N_2^+, and O_2^+.

NO^+ is produced by the following reactions:

$$N_2^+ + O \rightarrow NO^+ + N(^2D) \qquad (16)$$

$$O^+ + N_2 \rightarrow NO^+ + N(^4S) \qquad (17)$$

$$O_2^+ + NO \rightarrow NO^+ + N(^4S) \qquad (18)$$

$$O_2^+ + N(^4S) \rightarrow NO^+ + O \qquad (19)$$
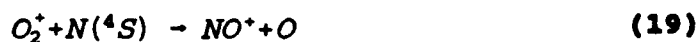
The following reactions lead to the loss of NO^+:

$$NO^+ + e \rightarrow O + N(^4S) \qquad (20)$$

$$NO^+ + e \rightarrow O + N(^2D) \tag{21}$$

Applying reactions (16) through (21), the density of NO^+ can be calculated from the following equation:

$$[NO^+] = \frac{K_{17a}[N_2^+][O] + K_{20}[O^+][N_2] + K_{22}[O_2^+][NO] + K_{23}[O_2^+][N(^4S)]}{[e](K_{26} + K_{27})} \tag{22}$$

The following reactions account for NO production:

$$N(^4S) + O_2 \rightarrow NO + O \tag{23}$$

$$N(^2D) + O_2 \rightarrow NO + O \tag{24}$$
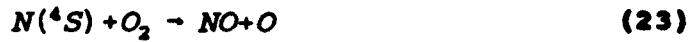
The reactions for NO loss are:

$$O_2^+ + NO \rightarrow NO^+ + O_2 \tag{25}$$

$$N(^4S) + NO \rightarrow N_2 + O \tag{26}$$

$$N(^2D) + NO \rightarrow N_2 + O \tag{27}$$

Combining reactions (23) through (27) yields the following calculation for the number density of NO:

$$[NO] = \frac{K_{28}[N(^4S)][O_2] + K_{29}[N(^2D)][O_2]}{K_{22}[O_2^+] + K_{33}[N(^4S)] + K_{34}[N(^2D)]} \tag{28}$$

18

The reactions for N(^{4}S) production are:

$$O + N_2 \rightarrow NO^+ + N(^4S) \tag{29}$$

$$NO + e \rightarrow O + N(^4S) \tag{30}$$

$$N(^2D) + e \rightarrow N(^4S) + e \tag{31}$$

$$N(^2D) + O \rightarrow N(^4S) + O \tag{32}$$

N(^{4}S) loss results from the following reactions:

$$O + N(^4S) \rightarrow NO^+ + O \tag{33}$$

$$N(^4S) + O_2 \rightarrow NO + O \tag{34}$$

$$N(^4S) + NO \rightarrow N_2 + O \tag{35}$$

Combining these equations in the form of equation (8) yields:

$$[N(^4S)] = \frac{K_{20}[O^+][N_2] + K_{26}[NO^+][e] + K_{30}[N(^2D)][e] + K_{31}[N(^2D)][O]}{K_{23}[O_2^+] + K_{28}[O_2] + K_{33}[NO]} \tag{36}$$

N(^{2}D) is produced by the following reactions:

$$N_2^+ + O \rightarrow NO^+ + N(^2D) \tag{37}$$

$$N_2^+ + e \rightarrow N(^2D) + N(^2D) \tag{38}$$

19

$$NO^+ + e \rightarrow O + N(^2D) \qquad (39)$$

The following reactions result in N(^{2}D) loss:

$$N(^2D) + O_2 \rightarrow NO + O \qquad (40)$$

$$N(^2D) + e \rightarrow N(^4S) + e \qquad (41)$$

$$N(^2D) + O \rightarrow N(^4S) + O \qquad (42)$$

$$N(^2D) + NO \rightarrow N_2 + O \qquad (43)$$
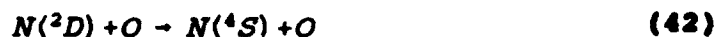
Combining equations (37) through (43) and solving for [N(^{2}D)] yields:

$$[N(^2D)] = \frac{K_{17a}[N_2^+][O] + K_{19}[N_2^+][e] + K_{27}[NO^+][e]}{K_{29}[O_2] + K_{30}[e] + K_{31}[O] + K_{34}[NO]} \qquad (44)$$

N_2^+ is produced by the following reaction:

$$N_2 + h\nu \rightarrow N_2^+ + e \qquad (45)$$

The following reactions result in N_2^+ loss:

$$N_2^+ + O \rightarrow NO^+ + N(^2D) \qquad (46)$$

$$N_2^+ + O \rightarrow O^+ + N_2 \qquad (47)$$

$$N_2^+ + O_2 \rightarrow O_2^+ + N_2 \tag{48}$$

$$N_2^+ + e \rightarrow N(^2D) + N(^2D) \tag{49}$$

Combining these reactions and solving for $[N_2^+]$ yields the following solution:

$$[N_2^+] = \frac{Q_{(N2)}}{K_{17a}[O] + K_{17b}[O] + K_{18}[O_2] + K_{19}[e]} \tag{50}$$

The following reactions lead to the production of O_2^+:

$$O_2 + h\nu \rightarrow O_2^+ + e \tag{51}$$

$$N_2^+ + O_2 \rightarrow O_2^+ + N_2 \tag{52}$$

$$O^+ + O_2 \rightarrow O_2^+ + O \tag{53}$$

The following reactions lead to the loss of O_2^+:

$$O_2^+ + NO \rightarrow NO^+ + O_2 \tag{54}$$

$$O_2^+ + N(^4S) \rightarrow NO^+ + O \tag{55}$$

$$O_2^+ + e \rightarrow O + O \tag{56}$$
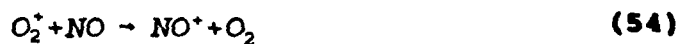
Combining reaction (51) through (56) results in the following solution:

$$[O_2^+] = \frac{Q_{(O2)} + K_{18}[N_2^+][O_2] + K_{21}[O^+][O_2]}{K_{22}[NO] + K_{23}[N(^4S)] + K_{24}[e]} \qquad (57)$$

The above equations are used in photochemical models such as the ones presented in Cleary (1986).

B. THE NIGHT AIRGLOW PHENOMENA

The night airglow spectrum has been extensively studied. Far ultraviolet measurements of the night airglow spectra have been assembled from several sources including Apollo 16, numerous rocketborne experiments, and several space shuttle and Skylab based experiments. The nature of the spectrum is well established. For the purposes of this paper, the far ultraviolet night airglow spectrum can be divided into two regions; 1000 - 1600Å and 1600 - 2000Å. This serves two purposes; first it separates the spectrum into the respective regions of coverage for the two cameras, and second, it separates the region of primarily oxygen related emissions from the region of primarily NO related emissions.

At night, the free ionospheric electrons and ions recombine resulting in a reduction of ion density. During this recombination process the atom or molecule can emit photons at various wavelengths. Figure (6) illustrates the night airglow spectra between 750 and 1400Å. This region is characterized by the spectra of O, O⁺, He, and H. Of note are the atomic oxygen recombination emission lines at 1304Å and

1356Å. These are the only significant emissions in the filtered Camera One passband.

Figure 6: Night Airglow Spectra between 750 - 1400Å obtained from STP78-1 at an Altitude of 600 km. (Rees pp 140)

Figure (7) shows the energy level diagram for OI. The transitions which are detectable by filtered Camera One cover the range from 10 to 7.5 eV.

The nightglow spectra of the 1600-2000Å region is characterized by the emissions of the NO-δ band. Figure (8) illustrates the nightglow spectrum from 1600 - 2950Å. Note the presence of two NO δ-band emissions below 2000Å. These are the only emissions detectable by filtered Camera Two, the upper limit of the camera prevents detection of NO γ-band emissions and allows the study of δ-band emissions only. Figure (9) shows the energy level diagram for NO. The passband of filtered Camera Two equates to potentials between

Singlets   Triplets   Quintets

$^1S_0$ $^1S_1$ $^1P_1$ $^1P_1$ $^1D_2$ $^1D_2$ $^1F_3$ $^1F_3$ $^3S_1$ $^3P_{210}$ $^3P_{210}$ $^3D_{123}$ $^3D_{123}$ $^5S_2$ $^5P_{3..1}$ $^5P_{3..1}$ $^5D_{..}$ $^5D_{..}$

Fig A3.1 Energy level diagram for OI showing the transitions that have been observed in the airglow or aurora.

Figure 7:   Energy Level Diagram for OI.
(Rees, Appendix 3)

7.75 to 6.2eV.   In Figure (9), the N and O atoms approach along the $a^4\Pi$ curve to the $C^2\Pi$ state.   The $C^2\Pi$ state decays to the ground $X^2\Pi$ state emitting the δ bands.   The reaction is:

$$N(^4S) + O(^3P) = NO(a^4\Pi) = NO(C^2\Pi) - NO(X^2\Pi) + h\nu \ (\delta\text{-}bands) \qquad (58)$$

The minima for the C and X states do not have the same internuclear separation.   This leads to the emission of several bands in the $v'=0$ transition. (Rees, pp.140-146)
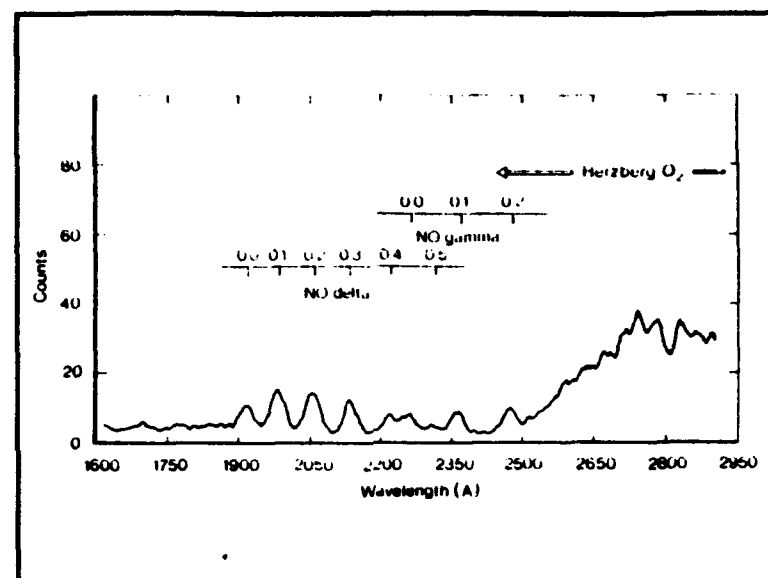
Figure 8: Nightglow Spectra from 1600 - 2950Å. Obtained from the S3-4 Satellite. (Rees pp141)
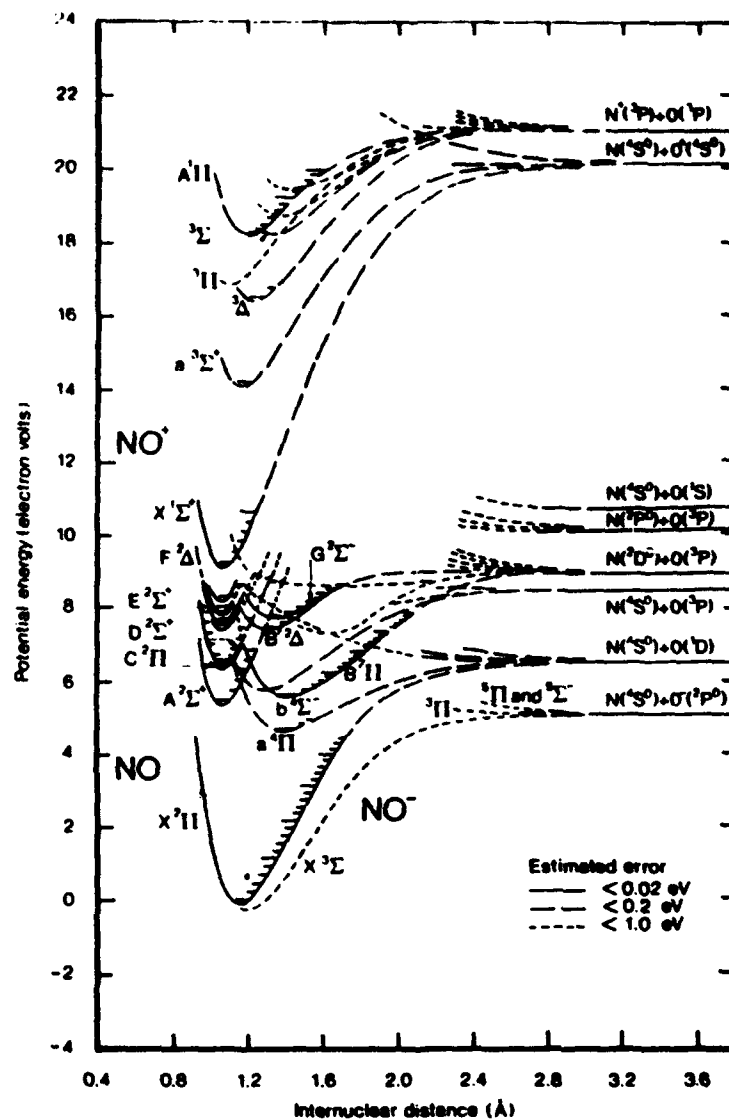
Figure 9: Energy Level Diagram for NO, NO⁺, and NO⁻. (Rees, Appendix 3)

III. THE FAR UV CAMERAS EXPERIMENT

The Naval Research Laboratory's Far UV Cameras Experiment was flown aboard STS-39 between April 28 and May 6 1991 as part of the Air Force Program 675 payload. The purpose of the Far UV cameras was to obtain images of the upper atmosphere, the shuttle environment, and celestial targets including stars and diffuse backgrounds. The wavelength band of the cameras was 1050Å to 2000Å. Two cameras were used to allow observations in two overlapping passbands; 1050 - 1600Å, and 1230 - 2000Å. Filters were used on some images to allow imaging in two distinct passbands; 1230-1600Å, and 1650-2000Å.

A. THE FAR UV CAMERAS

The electrographic Schmidt cameras developed at NRL are designed to provide for maximum sensitivity for detecting diffuse sources in the far UV range. This is accomplished through the use of (a) low f-number optics, (b) high efficiency opaque alkali halide photocathodes, and (c) microchannel intensification to permit detection of single photoelectron events. The objective was to develop from these far UV images a method by which an altitude profile of the upper atmosphere can be determined. Both cameras have aperture diameters of 75mm and a circular field-of-view of 20°

in diameter. The opaque alkali halide photocathodes have much higher quantum efficiencies in the vacuum ultraviolet than do common semitransparent photocathodes. As a result, the two cameras have extremely high overall detection efficiencies. The difference between the two cameras lies in their diffuse source detection capability and their operating wavelength region.

1. Camera One

Camera one covers the 1050 - 1600 Angstrom range. This camera uses a LiF Schmidt corrector plate and a KBr photocathode. The wavelength range can be limited to 1230-1600Å by using a CaF_2 filter. This permits the removal of the strong Lyman-α emissions at 1216Å from the image thereby preventing saturation of the image by this emission. Camera One does not have a microchannel plate (MCP) intensifier and therefore single photoelectron events are not detected by this camera. An MCP is not useful at this wavelength region because the intensity of Lyman-α nightglow is on the order of 2000 Rayleighs and an MCP would saturate unfiltered images. The diffuse source sensitivity of camera one expressed as units of optical density (on the processed film) per KiloRayleigh-second is estimated at 0.04 d/kR-sec at a wavelength of 1216Å.

2. Camera Two

The second camera covers the 1230-2000Å range. This camera uses a LiF$_2$ Schmidt corrector and a CsI photocathode. The range can be limited to 1650-2000Å using a SiO$_2$ filter. Photocathode detection efficiency versus wavelength is given in Figure (10). An (MCP) is used in Camera Two. This is required in order to intensify the night airglow of wavelengths longer than 1230Å where the typical intensity is less than 10 Rayleighs. The diffuse source sensitivity for camera two is estimated at 4.0 d/kR-sec at 1304Å Camera Two can detect a 1R emission of 1304Å light at an average density of .1 using an exposure time of 25 seconds. The longest exposure time was 100 seconds, therefore an emission intensity of .25R would be detectable by camera two. The minimum intensity of the far UV diffuse galactic background is about 2.5R when integrated over the camera two passband. The minimum intensity of the night O$^+$ recombination airglow (1356A) is about 1R. As a result of the MCP intensification, single photoelectron events are observable by camera two. (Carruthers,1992)
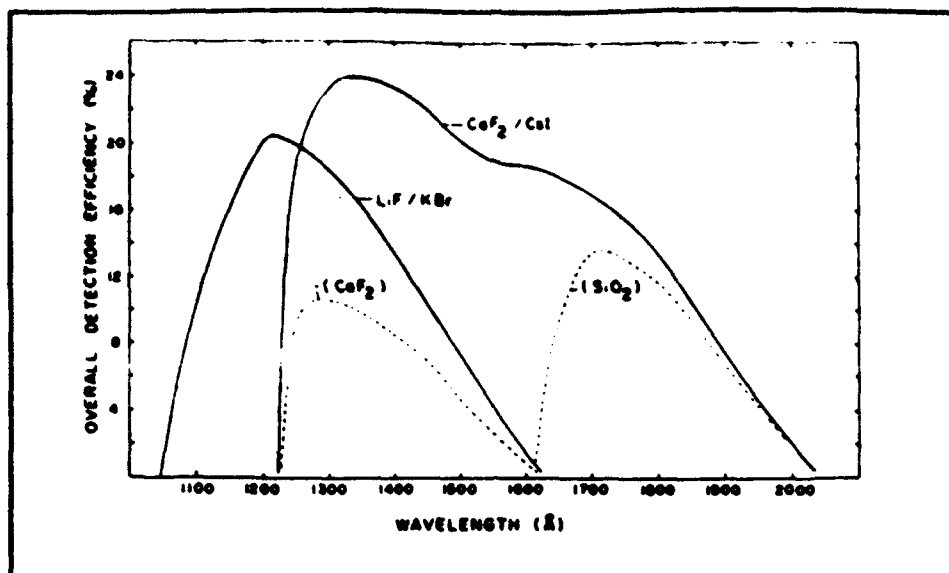
Figure 10: Photocathode Detection Efficiency vs Wavelength.

B. DATA REDUCTION

Nearly 400 images were recorded by the two cameras during the STS-39 mission. After flight the images were scanned into digital format using a microdensitometer. This instrument digitizes values of optical density d-$\log(I_o/I)$ where I_o and I are the incident and transmitted intensities of the scanning beam. The images were stored at NPS on a Sun Microsystem computer in the Flexible Image Transport System (FITS) format. The tapes are manipulated using Interactive Data Language (IDL).

30

IV. DATA ANALYSIS

A. FORMAT AND METHODS

1. Shuttle Position Data Files

The shuttle position data is contained on the Postflight Attitude Trajectory History (PATH) data tapes. The PATH data tapes used for this project are held at Naval Research Lab Washington DC, Space Science Division. The contents of the PATH data tapes are described in detail in NASA publication ICD-I-TOP-002 dated 15 January 1988. The required material from the tapes was obtained in November 1992. All required PATH data for each exposure taken during the PF03 block of the FAR UV cameras experiment is contained in each record. A PATH data record is recorded for every 10 seconds of flight except when transmission problems prevented reception. Although some breaks in data were experienced, the PATH tapes provide enough information to determine shuttle position and attitude accurately for each airglow image. A description of the data fields contained in each PATH record is contained in Appendix B.

a. Positional Analysis

The determination of where the center of each image is pointed is critical to this project. Specifically, the angle between the local vertical and the pointing

31

direction of the camera must be known. From this the observation zenith angle (OZA) can be determined for any point in the field-of-view. Therefore, the position and attitude of the orbiter must be determined. Two separate coordinate systems are used to define the position and attitude of the shuttle. The Aries-true-of-date system shown in Figure(11), and the orbiter body axis coordinate system. The Aries-true-of-date system is based on aligning the +x axis with the right ascension of the true-of-date equinox of Aries. The xy-plane is aligned with the true-of-date celestial equator. The +z axis is upward through true north, and the y-axis completes a right hand system. Right ascension is measured 0-360 degrees from the +x axis positive in the direction of the +y axis. Declination is the angle between the xy-plane and the radial vector to the orbiter and measured positive toward the +z axis and negative toward the -z axis. The position of Aries used in this system has been updated since the 1958 standard was established (hence, true-of-date). The SHPOS data field from the PATH data record gives the orbiter position in the Aries true-of-date coordinate system. Right ascension (RA) and declination (DEC) can be calculated from the xyz coordinates given in SHPOS.

The second system is the orbiter body-axis system. This system is illustrated in Figure (12). In this system the orbiter x-axis is aligned longitudinal to the body and is positive out the front of the orbiter. The z axis passes

through the center of gravity and is directed out the top and bottom of the orbiter normal to the x-axis. The z-axis is positive out the bottom of the orbiter. The shuttle y-axis is orthogonal to the xz-plane and completes a right hand system. The +y axis is directed outward toward the right wing.
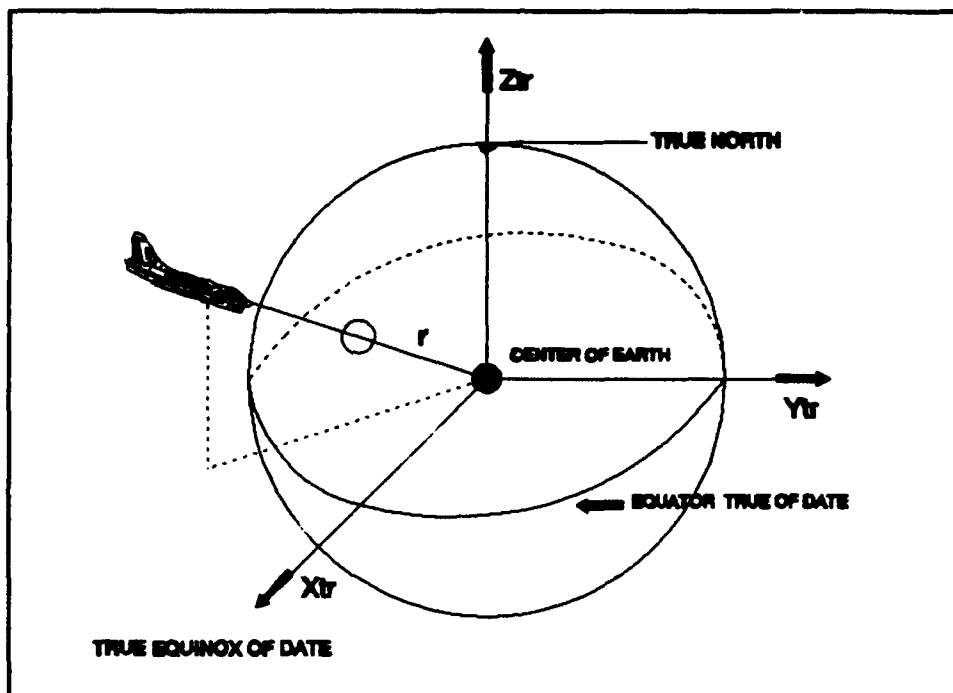

Figure 11: Aries True of Date Coordinate System.

The SHXRA and SHXDEC data fields give the aimpoint of the shuttle +x axis in terms of right ascension and declination. The SHZRA and SHDEC data fields give the aimpoint of the shuttle -z axis in terms of right ascension and declination.

Since the field-of-view is aligned with the orbiter -z axis, the orientation of the orbiter -z axis must be determined. The first step is to determine the orientation of the z-axis with respect to the orbiter radial (r). Using
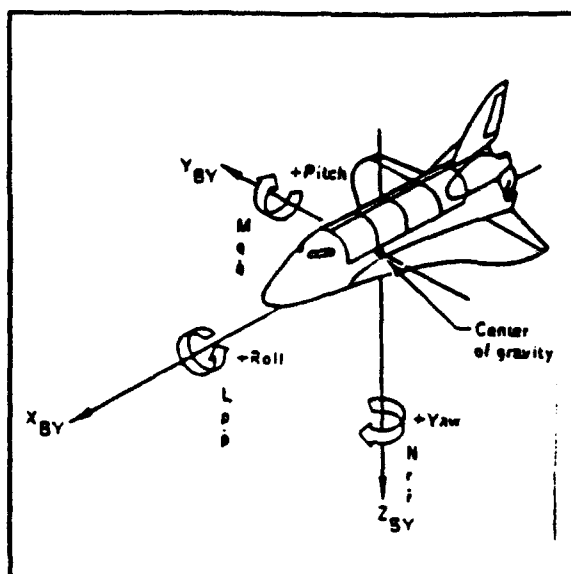
33

Figure 12: Orbiter Body Axis Coordinate System.

the unit vector defined by the RA and DEC of the orbiter, and the unit vector defined by the RA and DEC of the shuttle -z axis; the dot product of the two confirms the two vectors are orthogonal. This proves that the z-axis is orthogonal to the outward radial from the center of the earth. Using the Shuttle +x axis RA and DEC, the dot product of this vector and the radial confirm the two are parallel. Since both points pass through the shuttle position and are parallel the shuttle +x axis passes through the center of the earth. This verifies that the orbiter is nose down as expected. The final question is the position of the orbiter -z axis with respect to the Aries-true-of-date z-axis. To determine this, the RA and Dec of the orbiter, the RA and DEC of the orbiter -z axis, and the origin are used to define a plane containing the three points. The angle between this plane and the Aries-true-of-date +z

34

axis is the angle of the orbiter -z axis. Using a cross product of the two unit vectors to define a normal vector to the plane and the angle between the Aries-true-of-date +Z axis and the normal was calculated. This angle +/- 90 degrees gives the angle of the orbiter z-axis with respect to the Aries-true-of-date z-axis. Calculations confirmed the orbiter z-axis to be in the orbital plane which is at an inclination of 57 degrees. This confirms that the base of the shuttle was in the ram direction as expected. An illustration of orbiter attitude is given in Figure(13). Having confirmed the orientation of the field-of-view, the next step is to begin image processing.
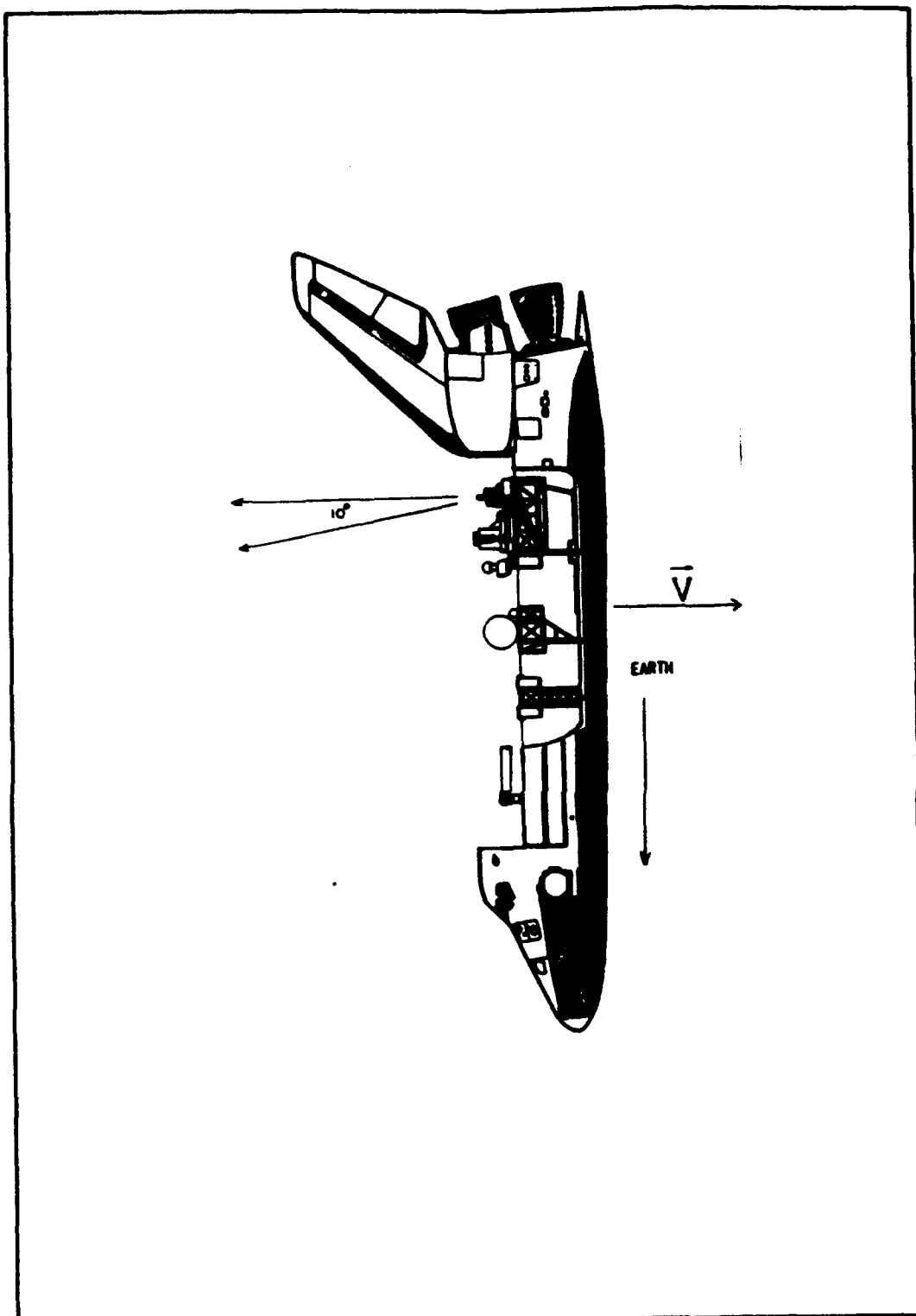
Figure 13: Orbiter Attitude for Airglow Images.
(Carruthers, 1992)

2. Image Processing

Image processing is performed using Interactive Data Language (IDL). The images were received from Naval Research Lab in the FITS format described above and were read using the IDL READFITS function. Four programs were developed. Three are required to recover data from an image. The fourth program is used to print output. The programs are contained in Appendix C.

The first program, **UVFILES.PRO**, is activated by typing **UVFILES,IMAGE** at the IDL prompt. **UVFILES.PRO** is the procedure-name and the parameter **IMAGE** is the variable name of the image. This parameter may have any name as long as it is consistent for all four procedures. This procedure allows the user to access the image using the IDL PICKFILE widget. Once selected, the image is read using the READFITS function and is rebinned from 2048 x 2048 to 512 x 512 to facilitate processing. The image array is divided by 800 to convert from photodensitometer output to density units. A 512 x 512 window is opened and the image is presented to the user in black and white. The screen will prompt the user to select a color table. Color table (13) (Rainbow) is recommended. For exposures of 30 seconds, color table (1) will also give a good visual presentation of the image.

Once the first program has run, the second program is called by typing **UVBACKGROUND,IMAGE**. This program allows the user to remove background noise form the image. Noise can be

imparted to the image file by the PDS procedure described in the data reduction section, by copying the files over a data net, and background effects from the film that was used. The UVBACKGROUND procedure allows the user to define a box by selecting two points with the mouse cursor. This is done in one of the four corners outside of the circular image. Care must be taken not to include any portion of the circular image in the box and not to include any artifact or defect which will skew results. The mean density unit value of this region is calculated and this value is subtracted from the image array. The new image replaces the old image in the view window.

The remaining two programs are called by typing either **UVCURSOR,IMAGE** or **UVCURSOR1,IMAGE**. These programs produce plots of intensity verses observation zenith angle. The only difference between the two programs is that UVCURSOR1 produces postscript files of the output graphs for printing. Both procedures will produce on screen graphs. After calling the program the user uses the mouse cursor left button to select points on the image. The points will be connected by a line to aid the user. Up to 512 points may be selected. When completed, press the right button to exit the cursor loop. The program then performs calibration calculations. The program asks for the number of seconds of the exposure and for calibration factors in Rayleighs and Photons. Calibration factors are listed in Table (1). The program then calculates

38

calibrated intensity values by multiplying the density units
for each point selected by the cursor by the calibration
factor and dividing by exposure time in seconds The UVCURSOR
procedures produce plots of intensity versus observation
zenith angle (OZA). OZA is based on the aimpoint of the
camera having an OZA of 90 degrees. The algorithm determines
the number of degrees per pixel based on a 20 degree field-of-
view and subtracts from a lower altitude limit of 100 degrees
OZA. For future research, a correction factor to account for
the camera aimpoint being not equal to 90 degrees can easily
be added to the program. For the benefit of the user, Two
plots are produced; the first gives intensity in Rayleighs,
the second plot is in Photons/sec/steradian/cm$^{2\cdot}$ The UVCURSOR
procedure can be run

Table I: FAR UV CAMERA CALIBRATION
FACTORS. R - RAYLEIGHS, PH - PHOTONS.

Camera	Filter	Factor
1	no	3.596168E4 R
1	no	2.858751E9 Ph
1	yes	6.263172E4 R
1	yes	4.978868E9 Ph
2	no	7.074304E2 R
2	no	6.623675E7 Ph
2	yes	4.444141E3 R
2	yes	3.532842E8 Ph

multiple times however the two plot windows must be quit
first. After running the UVCURSOR1 procedure the graphics
driver is set to postscript, this must be reset by the user to
the default driver for his system before additional image work
can be done. Therefore, the UVCURSOR1 procedure should be the
last one used for a given image, and only once the user is
ready for hardcopy plots. One additional plot is available;
a contour plot. This plot is produced by the procedure
UVCONTOUR and is called by typing UVCONTOUR,IMAGE. This plot
is in Rayleighs. As with UVCURSOR1, this procedure should be
run after UVBACKGROUND and the graphics driver must be reset
after the procedure is run.

B. RESULTS

Six airglow images were obtained from NRL, all are filterd
Camera Two images. The files are summarized in Table (II).

Table II: FAR UV FILENAMES, EXPOSURE LENGTHS, AND TIME OF
IMAGING.

Filename	Exposure Length	GMT
FARUV462.IFITS	3 seconds	05.04.16.21.59
FARUV143.IFITS	10 seconds	05.04.16.22.09
FARUV144.IFITS	30 seconds	05.04.16.22.39
FARUV62.IFITS	3 seconds	05.04.16.23.11
FARUV63.IFITS	10 seconds	05.04.16.23.21
FARUV55.IFITS	30 seconds	05.04.16.23.51

A color display of theses images is produced using
UVFILES,IMAGE. Figure (14) shows a contour plot of onr of
these images (FARUV144.IFITS). This plot was generated using
UVCONTOUR,IMAGE. Next, the orientation of the orbiter's +x
and -z axes were established. From this attitude information
a method for determining intensity versus observation zenith
angle was developed. A typical example of this is shown in
Figure (15). This figure shows the intensity profile
corresponding to the rectangular area in Figure (14). This
profile and printout was produced using UVCURSOR,IMAGE.
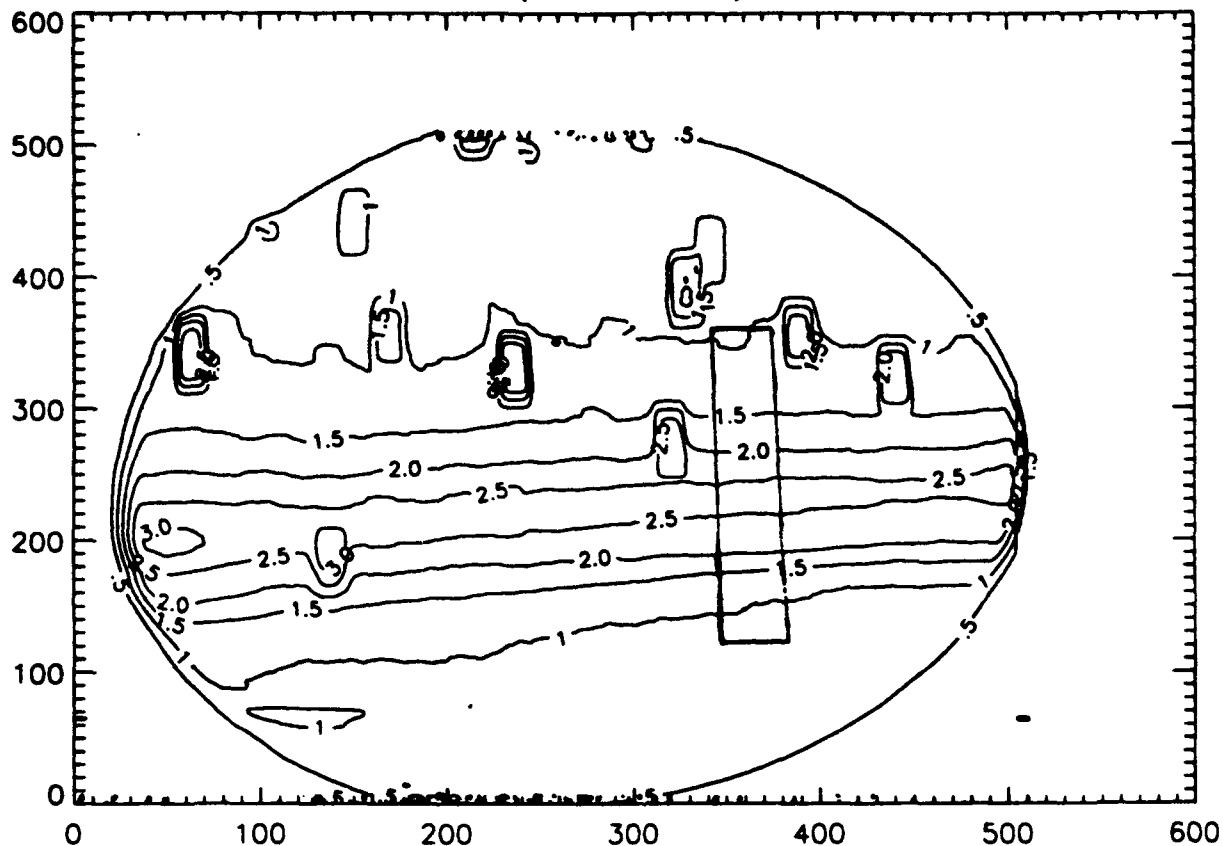
Contour Plot of Far UV Airglow Intensity
(Level x 100)

Figure 14: Contour Plot of Intensity vs Bin. Rectangular
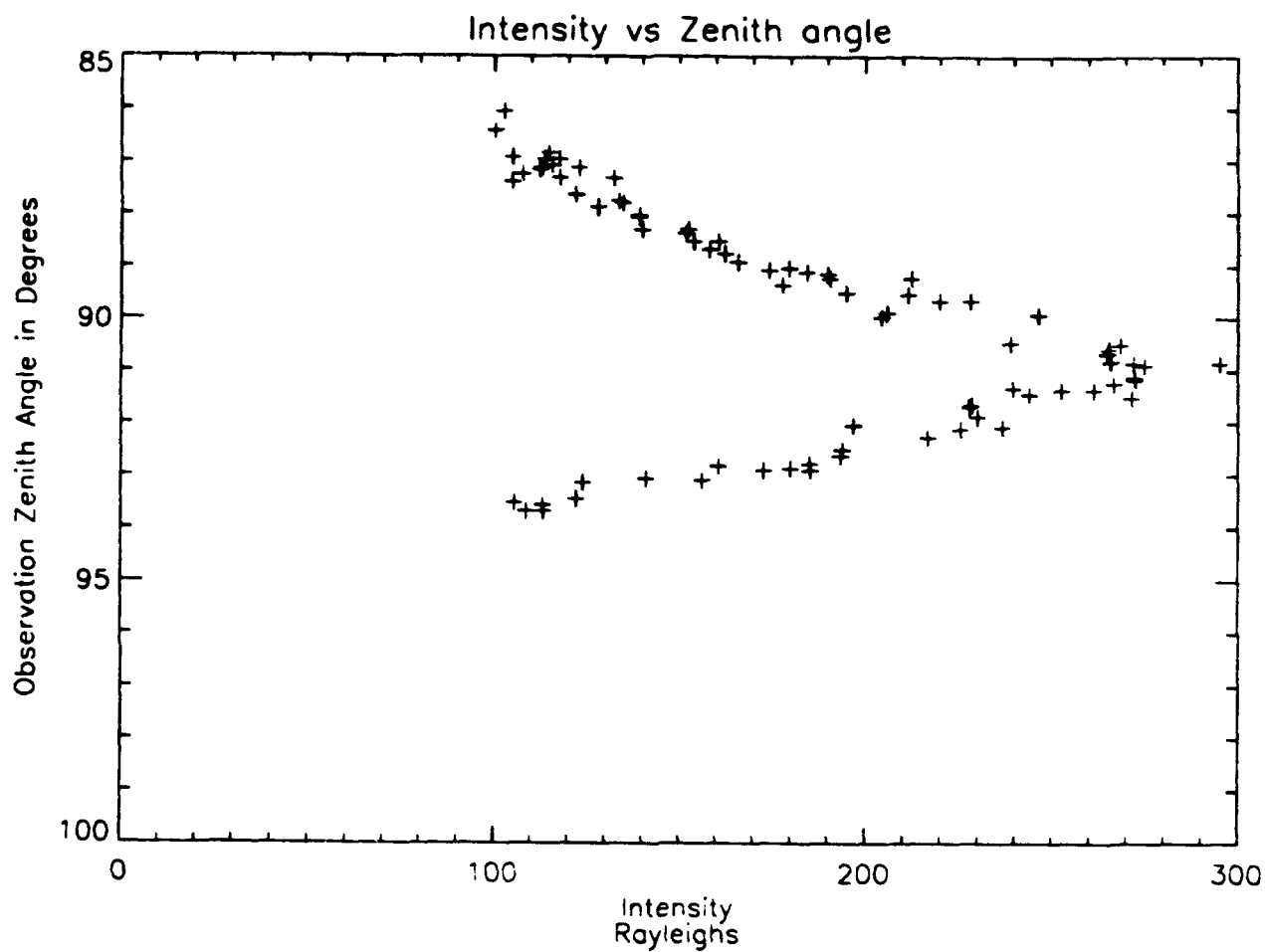Area shows the Vertical Column from which the Plot in
Figure (15) was derived.

42

Figure 15: Intensity vs OZA for the Area shown in Figure (14) above.

43

V. CONCLUSIONS

A. SUMMARY OF FINDINGS

Shuttle position and orientation has been established for six images of the Far Ultraviolet Cameras Experiment. All images are filtered Camera Two images. The orientation of the orbiter's +x and -z axes were established and from this a plot of intensity versus observation zenith angle was produced.

From these intensity plots, accurate measurements of thermospheric and ionospheric densities can be derived. From these densities an approximation of free electron density can be made. Since there are negligible numbers of negative ions; charge equilibrium requires that the number of positive ions equal the number of free electrons. Therefore, the density of positive ions equals the density of electrons. From this, a prediction of RF frequency effects can be made.

B. TOPICS FOR FURTHER STUDY

Since this is the first NPS thesis on the Far Ultraviolet Cameras Experiment, there are numerous topics for further research.

1. Determination of thermospheric/ionospheric densities from the intensity plots and relating them to geographic regions. This would include the removal of background radiation from celestial sources.

44

2.   Deriving an algorithm for processing the data from the Global Imaging Monitor of the Ionosphere satellite based upon the Far UV Camera images. Use of this algorithm to provide real time RF predictions to a geographic region.

3.   Spatial variations in charged particle densities in the ionosphere can be determined from spatial information in the images.

4.   Any topics concerning the aurora using six additional images of the aurora obtained form NRL. This will require additional position analysis as all aurora images were gimbled.

5.   Additional unfiltered images are available for work concerning Lyman-α effects and OI.

APPENDIX A: PCE REACTION RATES

Chemical Reaction Rates

This section contains all the chemical reactions and reaction rate coefficients used for the density calculation programs for the neutral atmosphere model. Sources for the equations are given on the last page of the appendix. Equation numbers correspond to those in Cleary (1986).

Chemical Reaction Rates (cont)

Number	Reaction	Rate (cm^3 s^{-1})
1	$O + h\nu \rightarrow O^+ + e$	$I_e = 9.1E{-}7$ s^{-1}
2	$O_2 + h\nu \rightarrow O_2^+ + e$	$I_e = 1.6E{-}6$ s^{-1}
3	$N_2 + h\nu \rightarrow N_2^+ + e$	$I_e = 1.2E{-}6$ s^{-1}
17a	$N_2^+ + O \rightarrow NO^+ + N(^2D)$	$1.4E{-}10$ $(T/300)^{-0.44}$
17b	$N_2^+ + O \rightarrow O^+ + N_2$	$1.0E{-}11$ $(T/300)^{-0.23}$
18	$N_2^+ + O_2 \rightarrow O_2^+ + N_2$	$5.1E{-}11$ $(T/300)^{-0.8}$
19	$N_2^+ + e \rightarrow N(^2D) + N(^2D)$	$1.8E{-}7$ $(T/300)^{-0.39}$
20	$O^+ + N_2 \rightarrow NO^+ + N(^4S)$	$5.0E{-}13$
21	$O^+ + O_2 \rightarrow O_2^+ + O$	$2.0E{-}11$ $(T/300)^{-0.4}$
22	$O_2^+ + NO \rightarrow NO^+ + O_2$	$4.4E{-}10$

Chemical Reaction Rates (cont)

Number	Reaction	Rate ($cm^3\ s^{-1}$)
23	$O_2^+ + N(^4S) \rightarrow NO^+ + O$	1.8E-10
24	$O_2^+ + e \rightarrow O + O$	1.0E-5 $(T)^{-0.7}$
26	$NO^+ + e \rightarrow O + N(^4S)$	.25*4.2E-7 $(T/300)^{-0.85}$
27	$NO^+ + e \rightarrow O + N(^2D)$	.75*4.2E-7 $(T/300)^{-0.85}$
28	$N(^4S) + O_2 \rightarrow NO + O$	4.4E-12exp(-3220/T)
29	$N(^2D) + O_2 \rightarrow NO + O$	6.0e-12
30	$N(^2D) + e \rightarrow N(^4S) + e$	6.0e-10 $(T/300)^{0.5}$
31	$N(^2D) + O \rightarrow N(^4S) + O$	5.0E-13
33	$N(^4S) + NO \rightarrow N_2 + O$	3.4E-11
34	$N(^2D) + NO \rightarrow N_2 + O$	7.0E-11

Sources of Chemical Reaction Rates

Equation number and source

1. Torr et al (1979)

2. Torr et al (1979)

3. Torr et al (1979)

17a. McFarland et al (1974)

17b. McFarland et al (1974)

18. Lindinger et al (1974)

19. Mehr & Biondi (1969)

20. Lindinger et al (1974)

21. McFarland et al (1973)

22. McFarland et al (1974)

23. Goldan et al (1966)

24. Torr et al (1976)

26. Torr et al (1976)   Kley et al (1977)

27. Torr et al (1976)   Kley et al (1977)

28. Becker et al (1969)

29. Lin & Kaufman (1971)

30. Frederick & Rusch (1977)

31. Rusch & Sharp (1981)

33. Lee et al (1978)

34. Black et al (1969)

APPENDIX B: PATH DATA FIELDS

This appendix contains a description of the data fields used in the Postflight Attitude Trajectory History. A more complete description of the entire PATH product can be found in the PATH product documentation provided by NASA.

Record number	Record
Orbit	Orbit number
GMT	YYMMDD.HHMMSS
ATTMAT	3x3 Transformation matrix.
SHPOS	Shuttle position in the Aries true of date coordinate system.
SHVEL	Shuttle Velocity components
SHXRA	Shuttle X axis right ascension
SHXDEC	Shuttle X axis declination
SHZRA	Shuttle +Z axis right ascension
SHZDEC	Shuttle +Z axis declination
SHLON	Shuttle Longitude
SHLAT	Shuttle Latitude
SHZSUN	Angle between shuttle +Z axis and Sun

SHZEAR	Angle between shuttle +Z axis and center of Earth
L$SNVS	0 - Sun not visible 1 - Sun visible
L$BBEC	0 - Not in Electrical contamination band 1 - In contamination band
TANRAD	Tangent radius

APPENDIX C: IMAGE PROCESSING PROGRAMS

This appendix contains IDL programs used to read the Far UV images and create the plots of intensity versus observation zenith angle.

```
pro uvfiles,image
file=pickfile(/read)

result=readfits(file,head)
image=rebin(result,512,512)
image=image/800.

window,1,xsize=512,ysize=512
tvscl,image
read,('select desired color table')
read,clrtbl
loadct,clrtbl

return
end
```

```
pro uvbackground, image


cursor, f, g, /device, /down
cursor, f1, g1, /device, /down

j=min([f,f1])
j1=max([f,f1])

k=min([g,g1])
k1=max([g,g1])

corner1=image(j:j1,k:k1)
area1=n_elements(corner1)
corner1=total(corner1)
corner1=corner1/area1




image=image-corner1
tvscl,image

return
end
```

```
pr       ,image

read,('use left mouse button to select point, press right button at last point')


cursor,x,y, /device, /down
counter=0
a=fltarr(512)
b=fltarr(512)


while (!err ne 4) do begin

        a(counter)=y
        b(counter)=image(x,y)

        cursor,x1,y1, /device, /down
        plots,[x,x1],[y,y1], /device

        counter=counter+1
        x=x1 & y=y1
endwhile




a=a(0:counter)
b=b(0:counter)

len=n_elements(a)-1

degrees=20./512.
za=100-(a*degrees)
read,('Enter exposure time in seconds:    '),seconds
read,('Enter Calibration Value for Rayleighs:    '),calfactor
read,('Enter Calibration Value for Photons:    '),photons

intensity=b*calfactor/seconds
intensityp=b*photons/seconds

window,0,xsize=512,ysize=512
plot,intensity,za,psym=1,$
        xrange=[min(intensity),max(intensity)],yrange=[max(za),min(za)],$
        title='Intensity vs Zenith angle',$
        xtitle='Intensity!cRayleighs/sec/steradian/cm^2',$
        ytitle='Observation Zenith Angle in Degrees'


window,2,xsize=512,ysize=512
plot,intensityp,za,psym=1,$
        xrange=[min(intensityp),max(intensityp)],yrange=[max(za),min(za)],$
        title='Intensity vs Zenith angle',$
        xtitle='Intensity!cPhotons/sec/steradian/cm^2',$
        ytitle='Observation Zenith Angle in Degrees'




return
end
```

```
pr   ...   ...   ...,....

rest,('use left mouse button to select point, press right button at last point')


cursor,x,y, /device, /down
counter=0
a=fltarr(512)
b=fltarr(512)


while (!err ne 4) do begin

        a(counter)=y
        b(counter)=image(x,y)

        cursor,x1,y1, /device, /down
        plots,[x,x1],[y,y1], /device

        counter=counter+1
        x=x1 & y=y1
endwhile




a=a(0:counter)
b=b(0:counter)

len=n_elements(a)-1

degrees=20./512.
za=100-(a*degrees)
read,('Enter exposure time in seconds:   '),seconds
read,('Enter Calibration Value for Rayleighs:   '),calfactor
read,('Enter Calibration Value for Photons:   '),photons

intensity=b*calfactor/seconds
intensityp=b*photons/seconds

window,0,xsize=512,ysize=512
plot,intensity,za,psym=1,$
        xrange=[min(intensity),max(intensity)],yrange=[max(za),min(za)],$
        title='Intensity vs Zenith angle',$
        xtitle='Intensity!cRayleighs/sec/steradian/cm^2',$
        ytitle='Observation Zenith Angle in Degrees'


window,2,xsize=512,ysize=512
plot,intensityp,za,psym=1,$
        xrange=[min(intensityp),max(intensityp)],yrange=[max(za),min(za)],$
        title='Intensity vs Zenith angle',$
        xtitle='Intensity!cPhotons/sec/steradian/cm^2',$
        ytitle='Observation Zenith Angle in Degrees'
```

55

```
set_plot,'ps'
device,filename='intenl.ps',/portrait

plot,intensityp,za,psym=1,$
        xrange=[min(intensityp),max(intensityp)],yrange=[max(za),min(za)],$
        title='Intensity vs Zenith angle',$
        xtitle='Intensity!cPhotons/sec/steradian/cm^2',$
        ytitle='Observation Zenith Angle in Degrees'

device,/close
```

```
device,filename='inten2.ps',/portrait

plot,intensity,za,psym=1,$
        xrange=[min(intensity),max(intensity)],yrange=[max(za),min(za)],$
        title='Intensity vs Zenith angle',$
        xtitle='Intensity!cRayleighs/sec/steradian/cm^2',$
        ytitle='Observation Zenith Angle in Degrees'

device, close
```

```
return
end
```

```
pro uvcontour,image

read,'enter exposure time in seconds',seconds
read,'enter Rayleigh calibration factor',cal

image1=image*cal/seconds
image1=smooth(image1,15)


set_plot,'ps'
device,filename='uvcontour.ps',/portrait

contour,image1,levels=[50,100,150,200,250,300],c_annotation=['.5','1','1.5','2.0','
title='Contour Plot of Far UV Airglow Intensity!c(Level x 100)'

device,/close

return
end
```

LIST OF REFERENCES

Carruthers,G.R., "The AFP-675 Far Ultraviolet Cameras Experiment: Observation of the Far UV Space Environment", Society of Photo-Optical Instrumentation Engineers, v.1764, 1992.

Carruthers,G.R., "The Far UV Cameras (NRL-803) Space Test Program Shuttle Experiment", Society of Photo-Optical Instrumentation Engineers, v.687, 1986.

Cleary,D.D., "Daytime High-Latitude Rocket Observations of the NO γ,δ, and ϵ Bands", Journal of Geophysical Research, 91,no. A10, 1986.

Heicklen,J., Atmospheric Chemistry, Academic Press, 1976.

Rees,M.H., Physics and Chemistry of the Upper Atmosphere, Cambridge University Press, 1989.

INITIAL DISTRIBUTION LIST

No. copies

1. Chairman, Electronic Warfare Academic Group   1
    Code EW
    Naval Postgraduate School
    Monterey, CA 93943-5000

2. Professor David D. Cleary, Code PH/CL   2
    Naval Postgraduate School
    Monterey, CA 93943-5000

3. Library, Code 52   2
    Naval Postgraduate School
    Monterey, CA 93943-5000

4. Professor Suntharalingam Gnanalingam   1
    Code PH/GN
    Naval Postgraduate School
    Monterey, CA 93943-5000

5. Lieutenant T. P. Hekman, USN   1
    Surface Warfare Officers School Command
    Department Head Course
    Newport, RI

6. Commanding Officer   1
    Naval Research Laboratory (Code 4109)
    ATTN: Dr George Carruthers
    Washington, D.C. 20375-5320

7. Director, Space and Elecrtronic Combat Division 1
    Code(N64)
    Space and Electronic Warfare Directorate
    Chief of Naval Operations
    Washington, D.C. 20350-2000

8. Director Technical Information Center   1
    Cameron Station
    Alexandria, VA 22304-6412